



HAL
open science

Well injectivity during CO₂ storage operations in deep saline aquifers–Part 1: Experimental investigation of drying effects, salt precipitation and capillary forces

Yannick Peysson, Laurent André, Mohamed Azaroual

► To cite this version:

Yannick Peysson, Laurent André, Mohamed Azaroual. Well injectivity during CO₂ storage operations in deep saline aquifers–Part 1: Experimental investigation of drying effects, salt precipitation and capillary forces. *International Journal of Greenhouse Gas Control*, 2014, 22, pp.291-300. 10.1016/j.ijggc.2013.10.031 . hal-00932767

HAL Id: hal-00932767

<https://brgm.hal.science/hal-00932767v1>

Submitted on 17 Jan 2014

HAL is a multi-disciplinary open access archive for the deposit and dissemination of scientific research documents, whether they are published or not. The documents may come from teaching and research institutions in France or abroad, or from public or private research centers.

L'archive ouverte pluridisciplinaire **HAL**, est destinée au dépôt et à la diffusion de documents scientifiques de niveau recherche, publiés ou non, émanant des établissements d'enseignement et de recherche français ou étrangers, des laboratoires publics ou privés.

1
2
3
4
5
6
7
8
9
10
11
12
13
14
15
16
17
18
19
20
21
22
23
24
25
26

Well injectivity during CO₂ storage operations in deep saline aquifers

1: Experimental investigation of drying effects, salt precipitation and capillary forces

Yannick Peysson^a, Laurent André^b, Mohamed Azaroual^b

^a*IFPEN, 1 et 4 Avenue de Bois-Préau, 92 852 Rueil-Malmaison Cedex – France*

^b*BRGM, Water, Environment and Ecotechnologies Direction, 3 Avenue Claude Guillemin, BP 36 009, F-45 060 Orléans Cedex 2 – France*

Submitted to

International Journal of Greenhouse Gas Control

Abstract

27
28
29
30
31
32
33
34
35
36
37
38
39
40
41
42
43
44
45
46
47
48
49
50

Carbon Capture and Storage (CCS) is a technique than can potentially limit the accumulation of greenhouse gases in the atmosphere. Well injectivity issues are of importance for CCS because the gas injection rate must be maintained at a high level (a million tonnes of CO₂ per year and per site) during the industrial operation period (30 to 40 years). The risk of altered permeability must therefore be determined in order to guarantee the sustainability and the security of the CO₂ geological storage. Injection of dry gas in deep saline aquifers might lead to near wellbore drying and salt precipitation. The solid salt might then reduce the rock permeability by clogging pores or by pore throat restriction. The objective of this paper is to present new experimental results on the drying of rocks induced by continuous injection of large amount of dry gas (N₂). The main goal of the study was to understand and model the physical processes that govern the decrease in water saturation in reservoir rocks.

Two types of sandstone were used to study slow and fast drying rates and capillary effects on drying. The experimental results evince the main physical parameters that control the key mechanisms. In a companion paper in this issue (André et al., 2013), we show that the continuous approach in the context of a compositional two-phase flow model can fairly well predict the saturation evolution in the near wellbore and the alteration in permeability due to salt precipitation.

Keywords: drying-out effects, coupled modelling, relative permeability, salt precipitation, capillary processes.

1. Introduction

Geological sequestration of CO₂ into deep saline aquifers is of interest because these geological formations represent a huge storage volume. However, they have been studied much less than mature oil & gas reservoirs. Injection of carbon dioxide into saline aquifers might involve some specific effects that could limit the gas injectivity. Different mechanisms could alter the permeability. One of the first studied is geochemical reactions due to CO₂ injection (Kaszuba et al., 2003; Johnson et al., 2004; Brosse et al., 2005; Iageneau et al., 2005; André et al., 2007, 2010). The dissolution of the carbon dioxide in water can induce mineral precipitation and dissolution. The rock porosity and permeability can then be modified depending mainly on the rock type but also on injection conditions (Bacci et al., 2011a). Another mechanism, much less studied, is drying and salt precipitation at the near wellbore. The dry injected gas, at low water-vapour partial pressure, will equilibrate with the groundwater and water mass transfer will occur leading to the desiccation of the rock. Drying effect has been studied in the context of oil & gas to estimate *water blocking* in the case of gas production well (Mahadevan et al., 2006, 2007) but drying can also induce salt precipitation in the case of saline aquifer. The solid salt might reduce the rock permeability by clogging pores or by pore throat restriction. This effect has been reported for gas producing wells in reservoirs of high salinity brine (Kleinitz et al., 2003). In the context of CO₂ geological storage, injectivity alteration by salt precipitation has been analytically and numerically studied by Giorgis et al. (2007), Pruess and Müller (2009), Pruess (2009) and Zeidouni et al. (2009). They showed that skin factors due to salt precipitation effects can be evaluated. Flow models have been used to study drying and precipitation dynamics in simplified well bore geometry taking into account a larger set of parameters (Spycher et al., 2003; Spycher and Pruess, 2005; André et al., 2007). The results reveal large drying zones in certain cases. Recent experimental work has attempted to measure the change in permeability under controlled drying conditions and has shown that permeability can alter significantly (Bacci et

78 al., 2011b; Ott et al., 2011; Peysson et al., 2011a; Peysson, 2012; Golghanddashi et al.,
79 2013).

80 The expansion with time of dried zones near injection wells has been studied for the most
81 part numerically, and field-scale comparison is not yet possible because few large-scale
82 pilots have been built. Experimental studies are therefore very useful for determining the key
83 parameters involved so that we can correctly model well injectivity in the context of CO₂
84 storage. We studied the effect of long-term injection of dry gas in brine-saturated rock
85 samples having different porosities and permeabilities in order to understand and quantify
86 the main parameters needed to develop a comprehensive model of CO₂ injection in real
87 situations. We specifically looked at different drying rates and capillary effects that might limit
88 the drying by using rock samples with very different permeabilities. In a companion paper in
89 this issue, we describe the use of reservoir numerical models to simulate drying and
90 precipitation dynamics. The numerical results are in good agreement with the experiments
91 described in this paper.

92 **2. Experimental set up**

93 **2.1 Set up**

94 The experiment involved placing cylindrical rock samples 6 cm long and 4.9 cm in diameter
95 in a horizontal Hassler cell (Fig. 1). The inlet of the core holder is connected to a gas
96 reservoir and the injection pressure controller. A back pressure of 50 bars was set at the
97 outlet. Outlet gas fluxes were measured with a gas flow meter after the back pressure and
98 the water outlet volume had been recorded using a burette. The pressure drop across the
99 sample was also recorded. The system temperature is thermostatically controlled. An X-ray
100 source and detector are placed on a translation rail that records the saturation profile along
101 the sample. Calibration under dry and fully saturated conditions allows the water saturation
102 measurements. Each saturation profile is obtained in 12 minutes.

103 **2.2 Rocks and Fluids**

104 Two types of sandstone with very different petrophysical properties were used for this study.

105 One is a Vosges Sandstone that is representative of a reservoir rock with 20-22% porosity
106 and a permeability of about 100 mD. The other is a Moliere Sandstone with a very low
107 permeability 10^{-2} mD and 14% porosity. The Moliere Sandstone, which cannot be considered
108 to be representative of a reservoir rock, was chosen to study the effect of capillary trapping
109 on drying dynamics since capillary effects are enhanced in tight systems, and to test the
110 model more broadly and specifically in the low drying rate regime. The rock properties are
111 summarized in Table 1.

112 ***Non-wetting fluid (Nitrogen)***

113 The non-wetting fluid used in this study is nitrogen (N_2) because we focused only on drying
114 mechanisms. CO_2 might have caused ancillary geochemical reactions and water-rock
115 interactions outside of the scope of this study. The key parameter needed to evaluate drying
116 dynamics is the water vapour concentration in the gas phase at thermodynamic equilibrium
117 under specific temperature and pressure conditions. The water vapour content is known for
118 different gas and water systems and specifically for water brine/ CO_2 (Spycher et al., 2003;
119 Spycher and Pruess, 2005). So, the results, in term of drying dynamic, obtained using N_2 can
120 be used for CO_2 storage based on reservoir modelling with appropriate thermodynamic
121 description of the carbon dioxide/brine system.

122 ***Brine***

123 Various brines were prepared for the experiments. With the Moliere sandstone, we used
124 mainly a mixture of salt representative of a Paris Basin brine at a high salinity of 160 g/L (KCl
125 4.12 g/L; $MgCl_2 \cdot 6H_2O$ 5.23 g/L; $CaCl_2 \cdot 2H_2O$ 22.00 g/L; NaCl 139.33 g/L; Na_2SO_4 0.52 g/L)
126 (Azaroual et al., 1997). For the Vosges sandstone, we used a mixture of aqueous KCl and KI
127 solutions. The latter is used to intensify the density contrast for X-ray measurements.

128 ***2.3 Methodology***

129 The rock sample cores were initially dried in an oven at 80 °C for at least 24 hours and
130 placed in the core holder. A first X-ray profile under dry conditions was acquired before the
131 sample was saturated with the brine. A second X-ray profile was acquired in order to

132 calibrate the X-ray absorption technique for saturation measurements. The initial water
133 permeability was then determined by measuring the flow rate and pressure. The nitrogen
134 was then injected under controlled pressure. The inlet pressure was fixed and the outlet gas
135 flow rate was measured. Saturation profiles were recorded repeatedly to measure the
136 evolution of brine saturation in the samples.

137

138 **3. Drying of Moliere Sandstone samples by gas injection**

139 The dynamics of drying by gas injection have been only poorly investigated by experiments
140 (Mahadevan et al., 2007; Peysson et al., 2011b). The main objective of our work was to
141 measure the evolution of water saturation with time in order to quantify the drying effect. Is
142 there a remaining water phase blocked by capillary effects? What effect does the dissolved
143 salt have on drying dynamics and rock permeability? These questions must be answered if
144 we wish to predict, for CO₂ sequestration, the temporal and spatial evolution of the dry zone
145 near the injection wells. The first set of experiments was done with tight sandstone to
146 increase the capillary effects and to investigate the drying dynamics.

147 **3.1 Drying conditions at the lab scale and experimental results**

148 We measured the evolution of the local and average liquid saturation in the Moliere sample.
149 The nitrogen injection was imposed in four steps (Fig. 2). The outlet pressure was set at 50
150 bars and two temperatures were studied: 90 °C and 120 °C.

151 The pressure was increased step-wise to study the effect of gas velocity on saturation and
152 drying dynamics. The average water saturation and the outlet gas flow rates for the two
153 temperatures are shown in Fig. 3, and the local saturation profiles are shown in Fig. 4.

154 At both temperatures, the mean water saturation decreased and the gas outlet flow rate
155 increased (Fig. 3). During the first two pressure plateaus, the predominant regime was a two-
156 phase immiscible displacement (piston effect) as the gas flow pushed the water out of the
157 rock sample. Thereafter, the gas flow rate was high enough to evacuate part of the water as
158 water vapour in the gas phase (last two plateaus). In this regime, the water saturation

159 decreased below the irreducible water saturation level ($S_{wi} = 16\%$). At the same time, the gas
160 flow rate increased significantly. At 90°C, water saturation reached zero, and at 120°C, it
161 reached a “residual signal”. In both experiments, the samples were, in fact, completely dry.
162 To check that, we removed the samples and let them dry in an oven with regular weighting.
163 In both cases, no mass losses were observed. The “residual signal” at 120 °C corresponds to
164 the presence of precipitated salt in the sample measured with the X-ray.

165 The temporal evolution of the water saturation profiles also shows two trends (Fig. 4). The
166 first two pressure steps are characteristic of two-phase immiscible displacement with a gas
167 breakthrough and a decrease of the water saturation with a capillary fringe. (Because of
168 diffraction effects, the two ends of the sample are fuzzy and we do not have the water
169 saturation measurements at the ends. However, we clearly see the increase in saturation at
170 the end of the sample.) However, for the last two pressures steps and at both temperatures,
171 the profiles tend to flatten out and the capillary fringe disappears. Moreover, no drying front is
172 observed until the end of the experiments, which means that capillary flows were strong
173 enough to homogenise the water profiles even at low saturation.

174 At the end of the experiments, we observe no residual signal at 90 °C aside from a small
175 effect at the entrance ($x < 5\text{mm}$), and a flat profile with a peak at the entrance at 120 °C. In
176 both cases, precipitated salt is present in the sample.

177 Permeability, measured at the end of the experiments, had decreased due to the presence of
178 salt. The final gas permeability was 37 and 50 % of the initial permeability at 90 °C and 120
179 °C, respectively. Every sample was weighed at the end of the experiment, but the small
180 mass changes just allow estimating a porosity change of about one point or less.

181 **3.2 Quantitative Interpretation - Two phase flow immiscible displacement**

182 The results are representative of gas injection for CO₂ storage in the sense that two coupled
183 mechanisms contribute to the changes in wellbore water saturation: viscous displacement
184 and drying. In order to fully interpret the experiments quantitatively, we studied the effect of
185 two-phase flow on the total water saturation evolution. Darcy's law model for two-phase flow

186 (Kulkarni et al., 2009) was used to calculate the evolution in saturation caused by the
 187 injection of gas at an imposed pressure. Two closure laws are required: the gas-water
 188 capillary pressure and the gas-water relative permeability curves (Fig. 5).

189 The drainage capillary pressure curve was measured using the centrifuge technique and
 190 modelled with the following equation (Fig. 5a):

$$191 \quad P_c(S_w) = -P_0 \ln(S^*) + P_t \quad (1)$$

192 where P_t and P_0 are parameters and $S^* = (S_w - S_{min}) / (S_{max} - S_{min})$ is the reduced water saturation
 193 ($S_{min} = 0.16$ and $S_{max} = 1$). Relative permeability curves for gas and water were calculated
 194 using the Corey equation (Fig. 5b).

$$195 \quad K_r^w = K_{max}^w (S^*)^{\alpha_w} \quad (2)$$

$$196 \quad K_r^g = K_{max}^g (1 - S^*)^{\alpha_g} \quad (3)$$

197 Although the effect of temperature on relative permeability has rarely been studied, some
 198 measurements are available for thermal enhanced oil recovery (Hamouda and Karoussi,
 199 2008). The relative permeability curves change little for a small range of temperatures. This
 200 can be interpreted, bearing in mind that these curves represent, for the most part, the
 201 geometrical restriction to the flow of one phase relative to the other. The distribution of the
 202 fluid in the porous structure depends on the capillarity and wettability. However, within a
 203 temperature range of 90 to 120 °C, the changes are small. We therefore considered no
 204 changes in the relative permeability curves for our experiments at 120 °C.

205 The capillary pressure curve can be represented as $P_c = 2 \cdot \sigma \cdot \cos\theta / \langle r \rangle$, where $\langle r \rangle$ is the
 206 average pore radius saturated with water for a given saturation. The temperature variation
 207 would then be given by the surface tension variation σ and the wettability that could be
 208 locally represented by a contact angle θ (or more precisely the cosines of this angle). In
 209 general, surface tension decreases with temperature (Guyon et al., 2001). For water-air
 210 systems, the decrease is relatively small between 90 and 120°C (60 to 55 mN/m). For the

211 wettability, we assume, in our case, strong water wet rock and no change with the
212 temperature. The gas is the non-wetting phase for the two temperatures. So at a first
213 approximation, we kept the capillary pressure curve constant for the case of 120 °C.

214 For the CO₂/brine system, surface tension and wettability measurements as a function of the
215 temperature have been reported recently (Chalbaud et al., 2009, 2010).

216
217 The Darcy two phase flow equations were solved numerically. The calculated gas flow rate
218 and the average water saturation inside the core were compared to the experimental data
219 (Fig. 3). This confirmed that the first two pressure plateaus are essentially two-phase flow
220 immiscible displacement. However, the two last plateaus in the experiments are dominated
221 by drying dynamics. Indeed, with only two-phase flow, saturation should have continued to
222 the irreducible water saturation ($S_{wi} = 0.16$ for these samples) but we observed a total
223 desaturation of the samples. We must therefore quantitatively consider the effect of water
224 evaporation.

225

226 **3.3 Quantitative interpretation: Thermodynamic aspect of drying**

227 To interpret the drying dynamics, we assumed that irreducible saturation was achieved after
228 the gas displacement. The liquid water mobility was therefore zero. The dry gas was injected
229 at a mass flow rate Q_g (Fig. 6). If we introduce the water vapour weight concentration at
230 equilibrium C (kg of water/ kg of gas), the mass balance gives the outlet water flow rate CQ_g :

231 The decrease in the saturation in the sample is then directly related to the gas flow rate:

$$232 \quad \frac{dS_w}{dt} = - \frac{C}{m_0} Q_{gaz} \quad (4)$$

233 where m_0 is the initial mass of water in the fully saturated sample.

234 In porous media, a classical assumption is to consider a local thermodynamic equilibrium so
235 that the water vapour concentration can be calculated at equilibrium (Puiggali and Quintard,
236 1992). Indeed, the latent heat of the vaporisation is in excess in the solid phase and the

237 pores are small enough so that gas diffusion is fast enough to homogenise the water vapour
 238 at the pore scale.

239 **Water vapour concentration**

240 Water vapour concentration can be defined by the molar fraction y (mol of water vapour/mol
 241 of gas) or by the mass concentration C (kg of water/kg of gas). The relationship between the
 242 two variables is the following:

$$C = y \frac{M_{H_2O}}{M_{gas}} \quad (5)$$

244 where M_{H_2O} is the molar mass of water and M_{gas} is the molar mass (kg/mol) of the water
 245 vapour and gas mixture. For nitrogen:

$$C = y \frac{M_{H_2O}}{(1-y)M_{N_2} + yM_{H_2O}} = y \frac{M_{H_2O}}{M_{N_2} \left[1 - y \left(1 - \frac{M_{H_2O}}{M_{N_2}} \right) \right]} \quad (6)$$

247 But in the case of drying under our thermodynamic conditions, y is very small (around 10^{-3})
 248 and the term

$$\left(1 - \frac{M_{H_2O}}{M_{N_2}} \right) = 0.36 \quad (7)$$

250 We could therefore simplify C to:

$$C = y \frac{M_{H_2O}}{M_{N_2}} \quad (8)$$

252 The water vapour molar fraction was estimated analytically using the Ideal Gas Law. Indeed,
 253 at equilibrium, we have:

$$y = \frac{P_s(\bar{T})}{P} \quad (9)$$

255 where \bar{T} and \bar{P} are the average pressure and temperature in the sample. Since we
 256 measured the volumetric flow rate in our experiments, we introduced β (kg/m³), the water
 257 vapour concentration (mass of water vapour by volume of gas), and can write:

$$258 \quad CQ_g = \beta Q_{gas}^v \quad (10)$$

259 where β depends only on the temperature:

$$260 \quad \beta = \rho_0 \frac{P_s(\bar{T})}{P_0} \frac{M_{H_2O}}{M_{gas}} \frac{T_0}{T} \quad (11)$$

261 For nitrogen, we calculated β as a function of temperature (Fig. 7) ($\rho_0 = 1.17$ kg/m³ at $T_0 = 20$
 262 °C and $P_0 = 1.013 \cdot 10^5$ Pa). The vapour pressure equilibrium equation is the Duperray
 263 correlation, which represents fairly well the water vapour curve up to the critical point ($P_C =$
 264 221.2 bar $T_C = 374.15$ °C):

$$265 \quad P_s(\bar{T}) = \left(\frac{\bar{T}}{100} \right)^4 \quad (12)$$

266 where T is °C.

267 We also calculated β for the real gas equation for nitrogen with CARNOT, thermodynamic
 268 software developed by IFPEN, from the Peng-Robinson equation of state. In this case, we
 269 have a weak pressure effect (Fig. 7).

270 Kelvin effect - Capillary contribution to the vapour concentration

271 Using low permeability sandstone enabled us to study capillary effects. First, we evaluated
 272 the contribution of the Laplace pressure on the liquid-vapour equilibrium. This can be
 273 evaluated from the Kelvin equation (Eq. (13)):

$$275 \quad P_s^c(T) = P_s(T)\varphi \quad (13)$$

$$276 \quad \text{and } \varphi = e^{-\frac{M_{H_2O} P_c(S)}{\rho R T}} \quad (14)$$

277 The water liquid-vapour equilibrium curve $P_s(T)$ is modified in porous media by the capillary
 278 pressure $P_c(S)$. The water is trapped in liquid form and the vapour concentration in the gas
 279 decreases. The higher the capillary pressure, the lower the water vapour concentration. But
 280 even in the Moliere sandstone, this effect was very weak, as shown by the dashed line in Fig.
 281 7 (the correction is made for ideal gases only). We used the capillary pressure curve
 282 measured for the Moliere sandstone (Fig. 5 5a).

283 **Saturation evolution in drying regime**

284 From Eq. (4), if drying is the predominant regime of water evacuation, we can calculate the
 285 average saturation evolution in our experiments:

$$286 \quad S_w(t) = S_w^i - \frac{\beta}{m_0} \int_0^t Q_g(t) dt \quad (15)$$

287 where Q_g is the flow rate measured at the outlet of the core. Fig. 8 compares the average
 288 water saturation remaining in the sample and the saturation calculated with Eq. (15) (at 120
 289 °C, we removed the residual signal due to the precipitated salt to have only the water
 290 saturation evolution). In Fig. 8a, we used different values of β ($\beta_1=0.31$; $\beta_2=0.4$; $\beta_3=0.2$) to
 291 compare with the data.

292 For the two temperatures studied, only one value of β enables a perfect estimation of the
 293 decrease in saturation. β could be measured by adjusting the saturation calculated with Eq.
 294 (15) and the experimental data.

295 This strong coupling between the measured gas flow rate and the average saturation was
 296 verified for all of the experiments and for the two rock types. For each experiment, in the
 297 predominant drying regime, Eq. (15) was used to calculate β and Fig. 9 shows the values
 298 measured for the different temperatures studied.

299 These results are very interesting because we see a very good match with β calculated with
 300 the Real Gas Law, and we can then conclude that the evaluation of β at equilibrium is valid

301 and that the Kelvin effect can be totally disregarded, as expected based on the model (Eq.
 302 (10)).

303 **Outlet gas flow rate prediction in the drying mode**

304 Because the average water saturation and the outlet gas flow rate are coupled in the drying
 305 mode (Eq. (15)), if we can determine the outlet gas flow rate from the imposed pressure, we
 306 can directly deduce the water saturation. For this, we need to know the shape of the gas
 307 relative permeability curve in the unusual range $[0 - S_{wi}]$.

308 For the two experiments at different temperatures, we could directly estimate the gas relative
 309 permeability curve from the experimental data. Indeed, as shown on the local saturation
 310 profile, in the drying stage, the saturation within the sample does not depend on the position
 311 x (Fig. 4). The average water saturation depends only on time $S_w(x,t) = S_w(t)$. Under these
 312 conditions, assuming no water mobility, we can write the Darcy law directly under weak
 313 compressibility hypotheses:

$$314 \quad \frac{\Delta P}{L} = \frac{\mu_g}{K_0 K_r^g(S_w(t))} \frac{Q_g(t)}{A} \quad (16)$$

315
 316 Because the pressure is constant during the plateau, we can calculate the evolution of the
 317 gas relative permeability with saturation by the ratio of Eq. (16) at two times:

$$318 \quad K_r^g(S_w) = K_r^g(S_w(t=0)) \frac{Q_g(t)}{Q_g(t=0)} \quad (17)$$

319 The recorded data at 90 °C and 120 °C are represented in Fig. 10.

320 The only constraint imposed is $K_r^g(S_w=0) = 1$ (We have to recover the sample permeability in
 321 monophasic flow). The two data sets merge on a single curve (Fig. 11) that is coherent with
 322 the first set of relative permeability values estimated from the first experimental phase (two-
 323 phase flow displacement) showing that relative permeability is an effective parameter of the
 324 problem.

325

326 The results of the Fig. 11 also confirm that, as expected, relative permeability curves do not
327 depend greatly on temperature in the 90 – 120 °C range.

328 **3.4 Contribution of the two predominant mechanisms to the water saturation decrease**

329 Fig. 12 shows the evolution of the average water saturation if only two-phase flow (black thin
330 line) or only drying (bold black line) are taken into consideration. The saturation was
331 calculated with Darcy two-phase flow model, as discussed in paragraph 3.2 (black thin line),
332 and, using the experimental outlet gas flow rate, we calculated the equivalent water
333 saturation evacuated through evaporation (with Eq. (11)). At the end, the mass balance of
334 water is respected to within 3 % (water displaced through two-phase flow with water
335 evaporated).

336

337 **4. Drying experiments with Reservoir rock samples (Vosges sandstone)**

338 4.1 Experimental results

339 The second set of experiments was done with Vosges sandstone – a type of rock
340 representative of a sandstone aquifer. The initial gas permeability of the sample was 74 mD
341 and the porosity 21.8 %. The brine was 35 g/L, a mixture of KCl (55 %wt) and KI (45 %wt). In
342 these experiments, the imposed pressure was reduced in order to stay within the range of
343 measurement of the gas flow rate of our system. We imposed three pressure plateaus (120
344 mbars, 800 mbars and 1500 mbars) and measured the gas flow rate and the saturation
345 evolution in the sample with time. The temperature was lowered a little to decrease the
346 evaporation rate (80 °C). The outlet pressure was 50 bars. As with the experiment at 120 °C
347 with the Moliere sandstone, a residual absorption was obtained by the end of the drying. This
348 time, we used this as the calibration signal for the dry state. We could then represent the
349 evolution of the average (Fig. 13) and local liquid saturation in the sample with time (Fig. 14).

350 The average water saturation (Fig. 13) follows the same trend as for the Moliere samples.
351 The first plateau is purely two-phase flow displacement with a rapid gas breakthrough (at t=5
352 hours) and a low gas flow rate. The second plateau is mixed, with a significant contribution of
353 drying. For the highest pressure, drying is very rapid, lasting only a few hours.

354 The saturation profiles along the sample also show the same trend as for the Moliere
355 sandstone (Fig. 14). The first profiles are typical of two phase flow displacement with a
356 capillary fringe close to the outlet of the sample. The profiles are then flatter and at the end of
357 the drying, we clearly see a drying front that moves from the sample inlet to the outlet. This is
358 due to the fact that the drying rate is much higher than in the previous cases and the water
359 flow does not have time to re-equilibrate the water saturation in the sample.

360 The drying front is observed only at the very end of the drying stage. At higher water
361 saturation, capillary back flows are strong enough to flatten the water saturation profiles. The
362 dissolved salt is transported in the water and accumulates near the injection surface. At the
363 end of the experiment, the X-ray absorption signal is very heterogeneous throughout the rock
364 sample (Fig. 15).

365 There is a very pronounced peak in the first 5 millimetres of the sample. The residual signal
366 is due to the salt precipitation induced by the drying. The permeability decreases 70 % due to
367 this salt deposition (22 mD at the end compared to an initial 74 mD).

368 This case was numerically modelled in detail, with the full coupling of drying and two-phase
369 flow displacement (André et al., 2013).

370 We also injected gas at a constant imposed pressure of 300 mbars into a sandstone core
371 initially fully saturated with a 150 g/L of KCl brine (Fig. 16). This caused total plugging of the
372 sample. No gas flow was observed after 46 h, which confirms the previous interpretation of a
373 salt accumulation near the injection surface that can be strong enough to block the gas flow.
374 This has also been confirmed by modelling (André et al., 2013).

375 **4.2 Interpretation - Discussion**

376 The drying of the brine-saturated cores was forced by a driven gas flow. The main
377 mechanisms can be divided into two steps, as already mentioned in the literature
378 (Mahadevan et al., 2007):

379 - **Step 1:** Dry gas pushes the pore water by a piston effect. The flows of the two
380 phases (gas and brine) are controlled by Darcy equations. This is observed
381 regardless of the initial permeability of the porous medium (Figs. 3 and 12). First,
382 most of the water is pushed out from the core (to the outlet), then water can flow in
383 the other direction (toward the column inlet) due to capillary effects. This process re-
384 equilibrates the water saturation inside the core and explains the flattening of the
385 curves observed mid-way through the experiments (Figs. 4 and 14). During this first
386 phase, water turns also to vapour in the gas because thermodynamic equilibrium is
387 reached as already emphasized. However, this process contributes little to the water
388 transport compared to advection. As a consequence, in this first step, there is only
389 little evaporation, therefore no oversaturation and salt does not precipitate.

390 - **Step 2:** The water saturation in the core is close to the irreducible water saturation.
391 Darcy brine flows are not predominant and evaporation becomes the main process
392 within the core causing the water to be evacuated. During this phase, most of the
393 water mass exchange takes place at the injection surface where the gas comes into
394 contact with the water. The decrease in water saturation at the injection surface
395 induces brine capillary back flow that transfers the brine toward the injection surface.
396 Salt accumulates near the injection surface and precipitates when saturation is
397 reached. This is observed in each experiment, although to a lesser extent with the
398 Moliere sandstone (see the residual X-ray profiles for both samples at the end of the
399 drying in Fig. 4 where there is also a small peak in the first 5 millimetres). Salt
400 precipitation is not homogeneous because drying can cause the dissolved ions to
401 flow toward evaporating surfaces (Huinink et al., 2002; Sgair et al., 2007; Guglielmi et
402 al., 2008; Peysson, 2012). The salinity of the brine plays a crucial role in the amount
403 of salt precipitated even if this mechanism is observed for all the salinities tested. In
404 the experiment with Vosges sandstone, the brine salinity is 5 times higher than in the

405 experiment with Moliere sandstone. The consequence is a massive precipitation of
406 salt close to the inlet of the core with a full clogging preventing any gas injection.

407 The processes occurring during this second step are complex because many have opposite
408 effects. To better understand the different processes, a Péclet number can be calculated to
409 provide information concerning the ratio between advective and diffusive transport (Huinink
410 et al., 2002; Sgair et al., 2007; Guglielmi et al., 2008):

$$411 \quad Pe = L\beta V / \rho\phi D \quad (18)$$

412 where L is the characteristic length, D the diffusion coefficient ($D = 10^{-10}$ m²/s for salt in
413 water), and V the gas velocity ($V = Q_g/S$). β is taken from Fig. 9.

414 During step 2 (i.e., the drying period) of the experiments with Moliere sandstone, the low
415 mean gas velocity (about 2-3 L/h) caused a very low evaporation rate. Capillary flow
416 continuously re-equilibrated the water saturation inside the core (water flowed toward the
417 sample inlet). At the same time, because of water evaporation near the injection surface, the
418 salt concentration increased, creating a salt gradient inside the column. However, the low
419 Péclet number (about 4 and 15 at 90 °C and 120 °C, respectively) suggests that salt diffusion
420 occurred inside the core (from the inlet toward the outlet) resulting in a rather homogeneous
421 distribution of salt throughout the column.

422 For the experiment with the Vosges sandstone, the mean gas velocity (Q_g) was about 3
423 L/min (Fig. 13). Consequently, the Péclet number is about 360, which suggests the
424 predominance of advective processes. Massive capillary flow carried salt toward the injection
425 surface where the water evaporation was very rapid because of the gas injection flow rate.
426 Like for the previous experiments, a salt gradient was created inside the core. However,
427 because the diffusive fluxes were negligible compared to the evaporation rate, salt
428 precipitated close to the injection surface, leading to heterogeneous salt deposits.

429

430

431 **Conclusion**

432 We ran experiments to study the mechanisms governing the saturation evolution at the near
433 wellbore of CO₂ injection wells. During the first stage of gas injection, two-phase flow
434 immiscible displacement is the main mechanism and water is pushed in the aquifer. This
435 phase could be modelled with Darcy two-phase flow models. Thereafter, the residual water
436 at the near wellbore might be transferred to the gas phase by thermodynamic exchanges.
437 Drying is then the predominant mechanism controlling the decrease in water saturation. The
438 drying rate is proportional to the gas velocity and the water vapour concentration in the gas
439 had to be estimated at equilibrium.

440 Any dissolved salt in the water can be transported by capillary flows induced by drying and
441 can even accumulate near the injection surface. The permeability can then be altered by
442 pore clogging. To correctly determine well injectivity, all of these mechanisms must be
443 included in models to calculate the near wellbore permeability and porosity changes with
444 time.

445 **Acknowledgement**

446 This work was carried out within the framework of the “Proche Puits” project, co-funded by
447 the French National Agency for Research (ANR). The authors thank Brigitte Bazin and
448 Elisabeth Rosenberg for fruitful discussions and Frederic Martin and Marie Claude Lynch for
449 their help in conducting the experiments. They are also grateful to all project partners
450 (TOTAL, GDF Suez, Schlumberger, Itasca, CNRS, University de Lorraine, University of Pau)
451 for allowing the publication of this work.

452 **References**

453 André, L., Audigane, P., Azaroual, M., Menjot A., 2007. Numerical modeling of fluid–rock
454 chemical interactions at the supercritical CO₂–liquid interface during CO₂ injection into
455 a carbonate reservoir, the Dogger aquifer (Paris Basin, France), Energy Conversion
456 and Management 48, 1782–1797.

457 André, L., Peysson, Y., Azaroual, M., 2013. Well injectivity during CO₂ injection in deep
458 saline aquifers - Part 2: Numerical simulations of drying, salt deposit mechanisms and
459 role of capillary forces. *International Journal of Greenhouse Gas Control*, same issue.

460 Azaroual, M., Fouillac, C., Matray, J.M., 1997. Solubility of silica polymorphs in electrolyte
461 solutions, II. Activity of aqueous silica and solid silica polymorphs in deep solutions
462 from the sedimentary Paris Basin. *Chemical Geology* 140, 167-179.

463 Bacci, G., Korre, A., Durucan, S., 2011a. An experimental and numerical investigation into
464 the impact of dissolution/precipitation mechanisms on CO₂ injectivity in the wellbore
465 and far field regions, *International Journal of Greenhouse Gas Control* 5, 579-588.

466 Bacci, G., Korre, A., Durucan, S., 2011b. Experimental investigation into salt precipitation
467 during CO₂ injection in saline aquifer, *Energy Procedia* 4, 2011, 4450-4456

468 Brosse, É., Magnier, C., Vincent, B., 2005. Modelling Fluid-Rock Interaction Induced by the
469 Percolation of CO₂-Enriched Solutions in Core Samples: the Role of Reactive Surface
470 Area, *Oil & Gas Science and Technology - Rev. IFP* 60(2), 287-305.

471 Chalbaud, C., Robin, M., Lombard, J.M., Martin, F., Egermann, P., Bertin, H., 2009.
472 Interfacial tension measurements and wettability evaluation for geological CO₂ storage.
473 *Advance in Water Resources* 32, 98–109.

474 Chalbaud, C., Robin, M., Lombard, J.M., Bertin, M., Egermann, P., 2010. Brine/CO₂
475 Interfacial Properties and Effects on CO₂ Storage in Deep Saline Aquifers. *Oil & Gas
476 Science and Technology – Rev. IFP* 65 (4), 541-555.

477 Giorgis, T., Carpita, M., Battistelli, A., 2007. 2D modeling of salt precipitation during the
478 injection of dry CO₂ in a depleted gas reservoir. *Energy Conversion and Management*
479 48, 1816-1826.

480 Golghanddashti, H., Saadat, M., Abbasi, S., Shahrabadi, A., 2013. Experimental
481 investigation of water vaporization and its induced formation damage associated with
482 underground gas storage, *Journal of Porous Media*, 16(2), 89-96.

483 Guglielmini, L., Gontcharov, A., Aldykiewicz, J., Stones, H.A., 2008. Drying of salt solutions
484 in porous materials: Intermediate-time dynamics and efflorescence. *Physics of Fluids*,
485 20, 077101.

486 Guyon, E., Hulin, J.P., Petit, L., 2001. *Hydrodynamique Physique*, EDP Sciences CNRS
487 Editions.

488 Hamouda, A., Karoussi, O., 2008. Effect of temperature, wettability and relative permeability
489 on oil recovery from oil-wet chalk. *Energies* 1 (1), 19–34.

490 Huinink H.P.H., Pel, L., Michels, M.A.J., 2002. How ions distribute in a drying porous
491 medium: A simple model. *Physics of Fluids* 14 (4), 1389-1395.

492 Johnson, J.W., Nitao, J.J., Knauss, K.G., 2004. Reactive transport modelling of CO₂ storage
493 in saline aquifers to elucidate fundamental processes, trapping mechanisms, and
494 sequestration partitioning. Lawrence Livermore National Laboratory, UCRL-JRNL-
495 205627.

496 Kaszuba, J.P., Janecky, D.R., Snow, M.G., 2003. Carbon dioxide reaction processes in a
497 model brine aquifer at 200°C and 200 bars: implications for geologic sequestration of
498 carbon. *Applied Geochemistry* 18, 1065–1080.

499 Kleinitz, W., Dietzsch, G., Köhler, M., 2003. Halite scale formation in gas producing wells.
500 *Chemical Engineering Research and Design* 81 (Part A).

501 Kulkarni, R., Watson, A.T., Nordtvedt, J.E., Sylte, A., 1998. Two-Phase Flow in Porous
502 Media: Property Identification and Model Validation. *AIChE Journal* 44 (11), 2337-2350.

503 Lagneau, V., Pipart A., Catalette H., 2005. Reactive transport modelling of CO₂ sequestration
504 in deep saline aquifers. *Oil & Gas Science and Technology – Rev. IFP* 60(2), 231–247.

505 Mahadevan, J., Sharma, M.M., Yortsos, Y.C., 2006. Flow-Through drying of porous media,
506 *AIChE Journal* 52, 2367–2380.

507 Mahadevan, J., Sharma, M.M., Yortsos, Y.C., 2007. Water removal from porous media by
508 gas injection: experiments and simulation. *Transport in Porous Media* 66, 287-309.

509 Ott, H., de Kloe, K., Marcelis, F., Makurat, A., 2011. Injection of Supercritical CO₂ in brine
510 saturated sandstone: pattern formation during salt precipitation, *Energy Procedia* 4,
511 4425-4432.

512 Peysson, Y., Bazin, B., Magnier, C., Kohler, E., Youssef, S., 2011a. Permeability alteration
513 due to salt precipitation driven by drying in the context of CO₂ injection. *Energy*
514 *Procedia* 4, 4387-4394.

515 Peysson, Y., Fleury, M., Blázquez-Pascual, V., 2011b. Drying Rate Measurements in
516 Convection- and Diffusion-Driven Conditions on a Shaly Sandstone Using Nuclear
517 Magnetic Resonance. *Transport in Porous Media* 90 (3), 1001-1016.

518 Peysson, Y., 2012. Permeability alteration induced by drying of brines in porous media. The
519 European Physical Journal - Applied Physics 60, 24206p1-p12.

520 Pruess, K., Müller, N., 2009. Formation dry-out from CO₂ injection into saline aquifers: 1.
521 Effects of solids precipitation and their mitigation, Water Resources Research 45,
522 W03402.

523 Pruess, K., 2009. Formation dry-out from CO₂ injection into saline aquifers: 2. Analytical
524 model for salt precipitation, Water Resources Research 45, W03403.

525 Puiggali, J.R., Quintard, M., 1992. Properties and simplifying assumptions for classical drying
526 models. Advances in Drying, Publisher: Hemisphere Publishing Corporation, Chapter
527 4, 109-143.

528 Sghair, N., Prat, M., Ben Nasrallah, S., 2007. On ions transport during drying in a porous
529 medium. Transport in Porous Media 67, 243-274.

530 Spycher, N., Pruess, K., Ennis-King, J., 2003. CO₂-H₂O mixtures in the geological
531 sequestration of CO₂ I. Assessment and calculation of mutual solubilities from 12 to
532 100°C and up to 600 bar. Geochimica et Cosmochimica Acta 67 (16), 3015-3031.

533 Spycher, N., Pruess, K., 2005. CO₂-H₂O mixtures in the geological sequestration of CO₂ II.
534 Partitioning in chloride brines at 12 to 100°C and up to 600 bar. Geochimica et
535 Cosmochimica Acta 69 (13), 3309–3320.

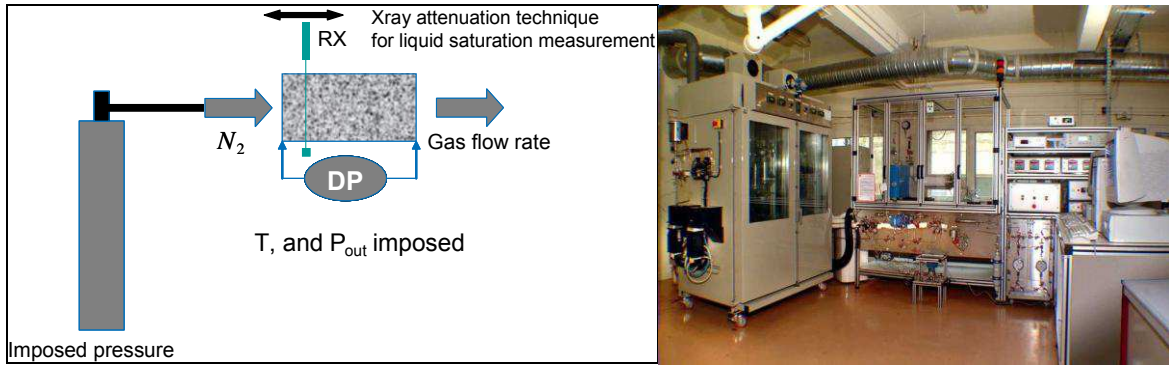
536 Zeidouni, M., Pooladi-Darvish, M., Keith, D., 2009. Analytical solution to evaluate salt
537 precipitation during CO₂ injection in saline aquifers. International Journal of
538 Greenhouse Gas Control 3, 600-611.

539
540

541
542
543
544
545
546
547
548
549
550
551
552
553
554
555
556
557
558
559
560
561
562
563
564
565
566
567
568
569
570

List of Illustrations

- Fig. 1: Experimental set up.
- Fig. 2: Pressure steps in the two experiments
- Fig. 3: Average water saturation evolution vs. time and outlet gas flow rate. Solid line and small connected triangles: two-phase flow model.
- Fig. 4: Water saturation profiles along the sample with time: (a) at 90°C; (b) at 120°C.
- Fig. 5: (a) Measured capillary pressure curves (J2, K2, K3, and L1 are 4 samples measured using the centrifuge technique) and model = bold black line; (b) Relative permeability curves for two phase flow immiscible displacement calculated using the Corey equation.
- Fig. 6: The mass balance for desaturation by drying
- Fig. 7: Water vapour concentration β as a function of temperature. Ideal Gas Law (thin black line); Real Gas Law (thick black line at 50 bars, thick grey line at 100 bars). Kelvin correction in the case of low permeability samples (dashed line).
- Fig. 8: Average water saturation evolution as a function of time in the last pressure plateau for the two temperatures studied, 90 °C (a) and 120 °C (b).
- Fig. 9: β variation with temperature.
- Fig. 10: Average water saturation and gas flow rate at (a) 90 °C and (b) 120 °C.
- Fig. 11: Extension of the gas relative permeability K_{rg} for saturation in the range $[0 - S_{wi}]$.
- Fig. 12: Average sample water saturation and outlet gas flow rate. Simulation of the saturation decrease with two-phase flow model (black thin line). Water evacuated by the gas flow (equation 11 represented as saturation) (bold black line). Total contribution = sum of the two effects (white dots).
- Fig. 13: Experimental average water saturation (black dots) and experimental gas flow rate (white dots) as a function of time for the Vosges Sandstones for 3 steps of inlet pressures.
- Fig. 14: Water saturation profiles along the sample with time.
- Fig. 15: X-ray residual signal as a function of the position x in the sample.
- Fig. 16: Average water saturation and gas flow rate

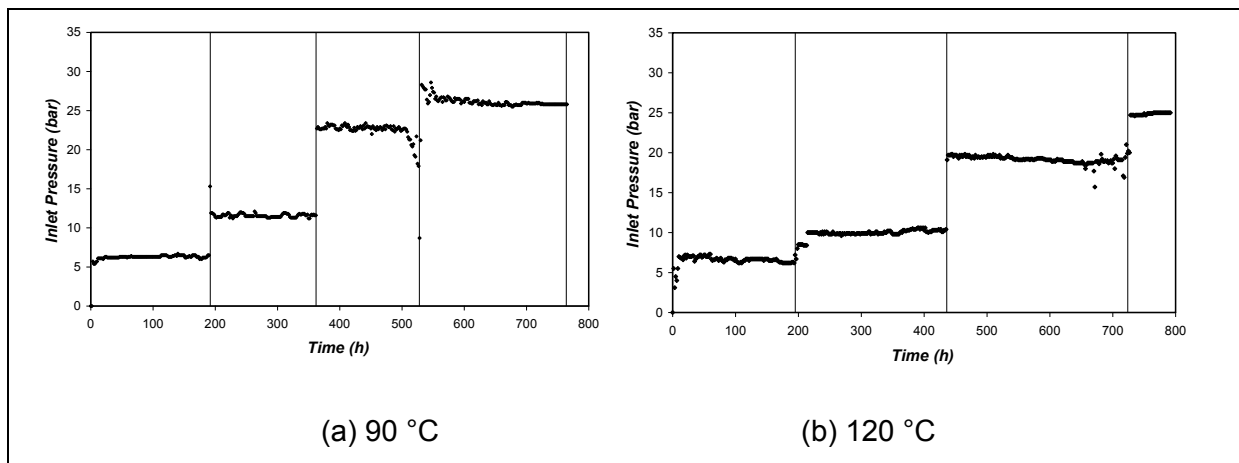


571

572

573

Fig. 1



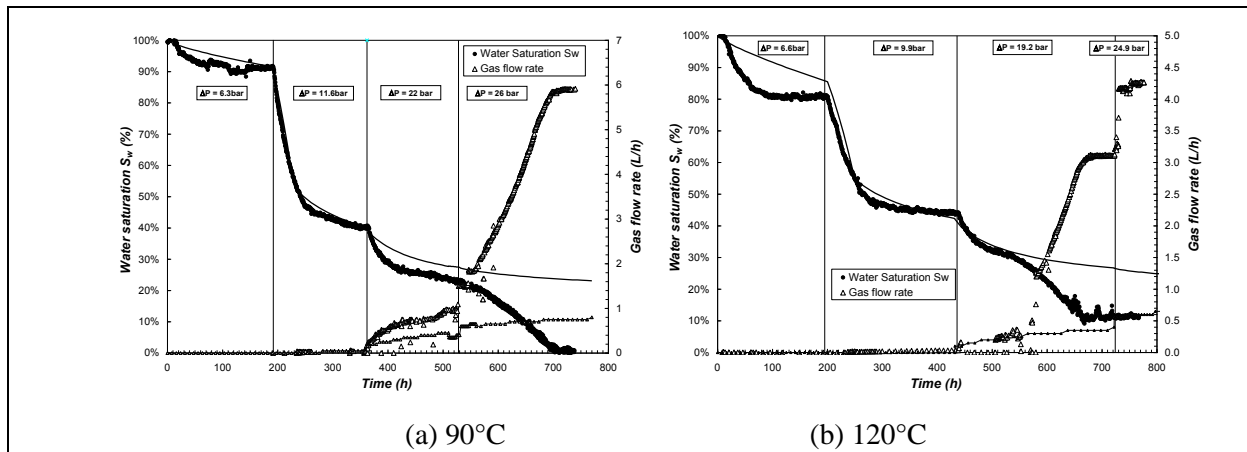
574

575

576

577

Fig. 2



578

579

580

581

Fig. 3

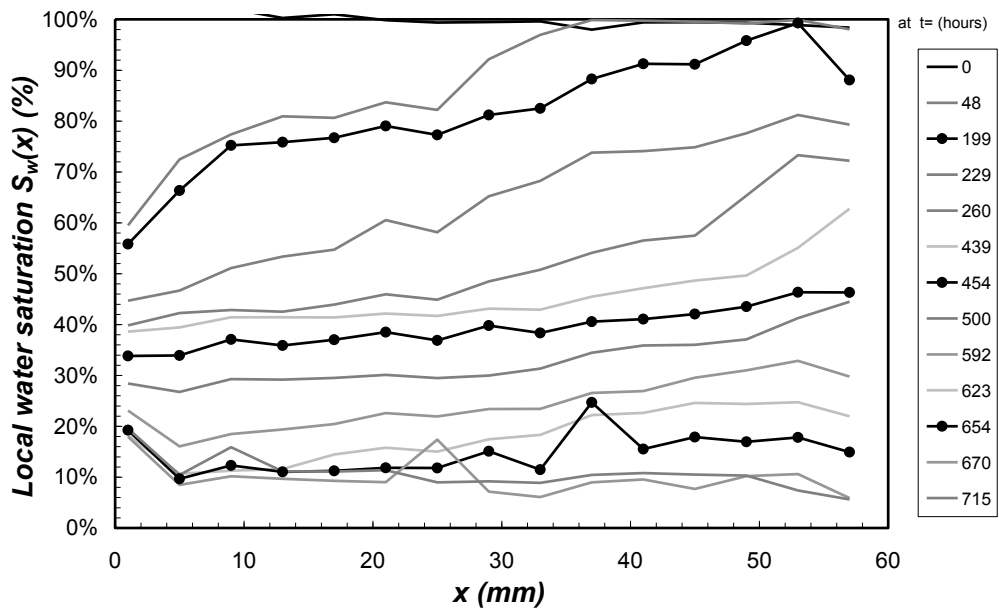
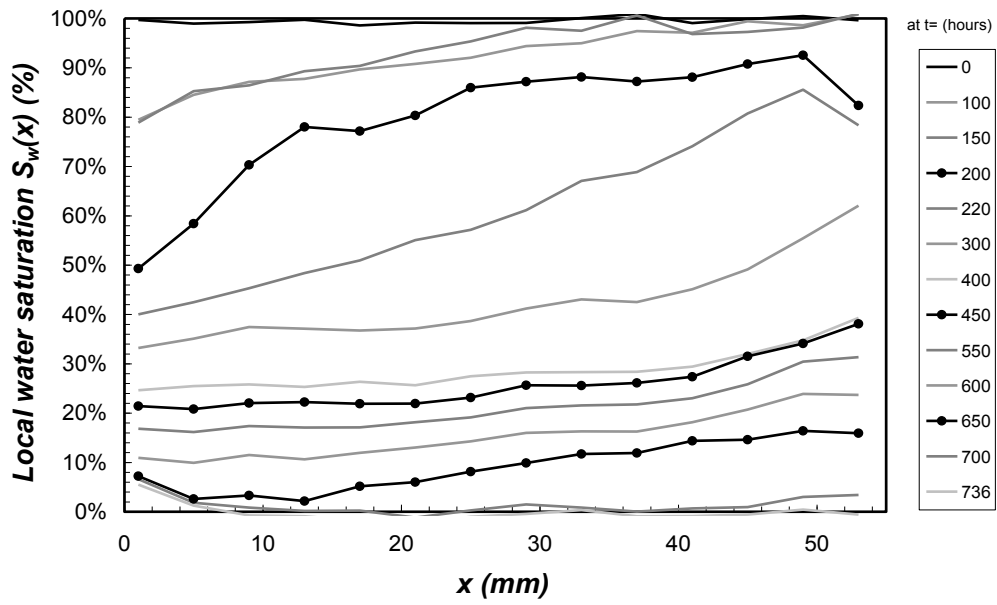


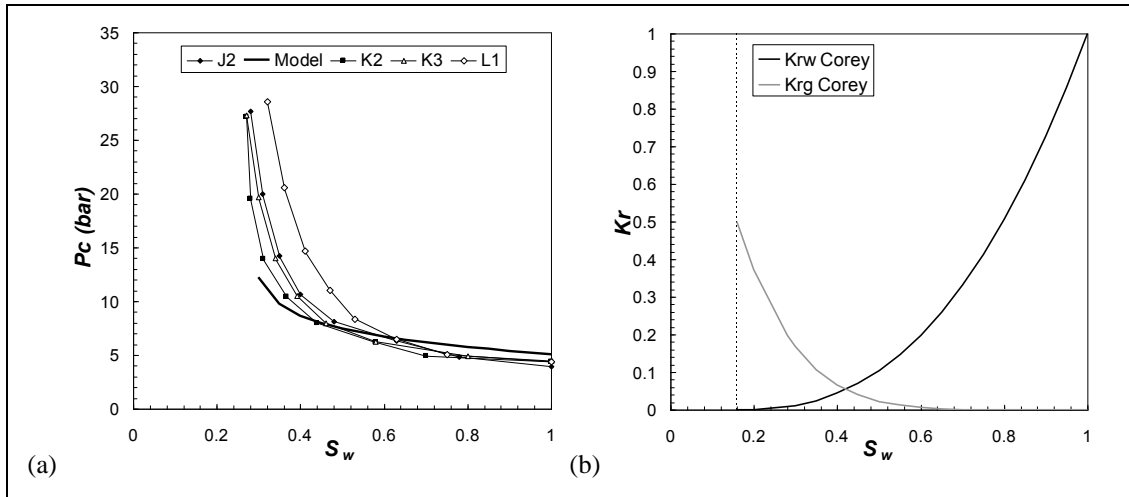
Fig. 4

582

583

584

585

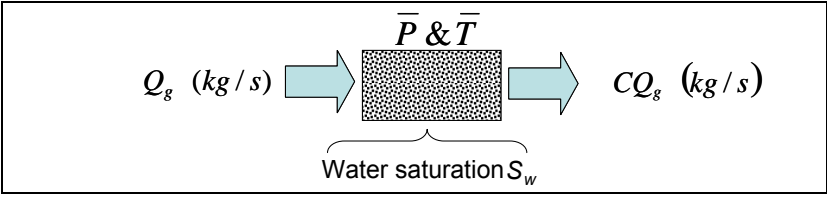


586

587

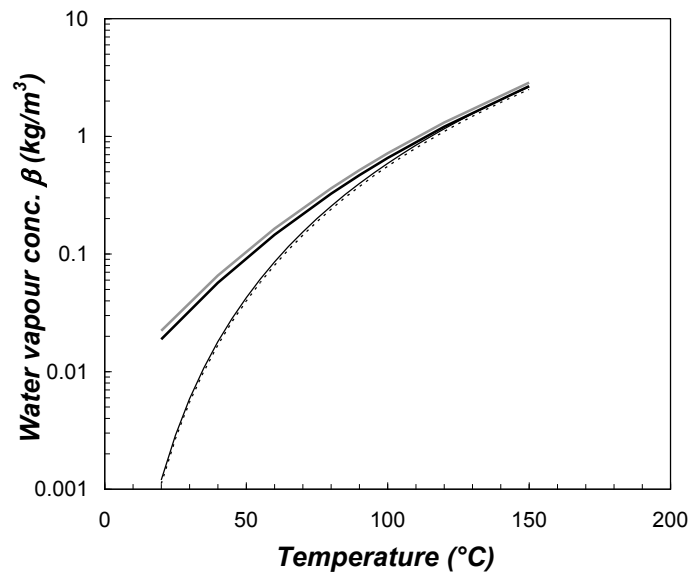
588

Fig. 5



589
590
591

Fig. 6

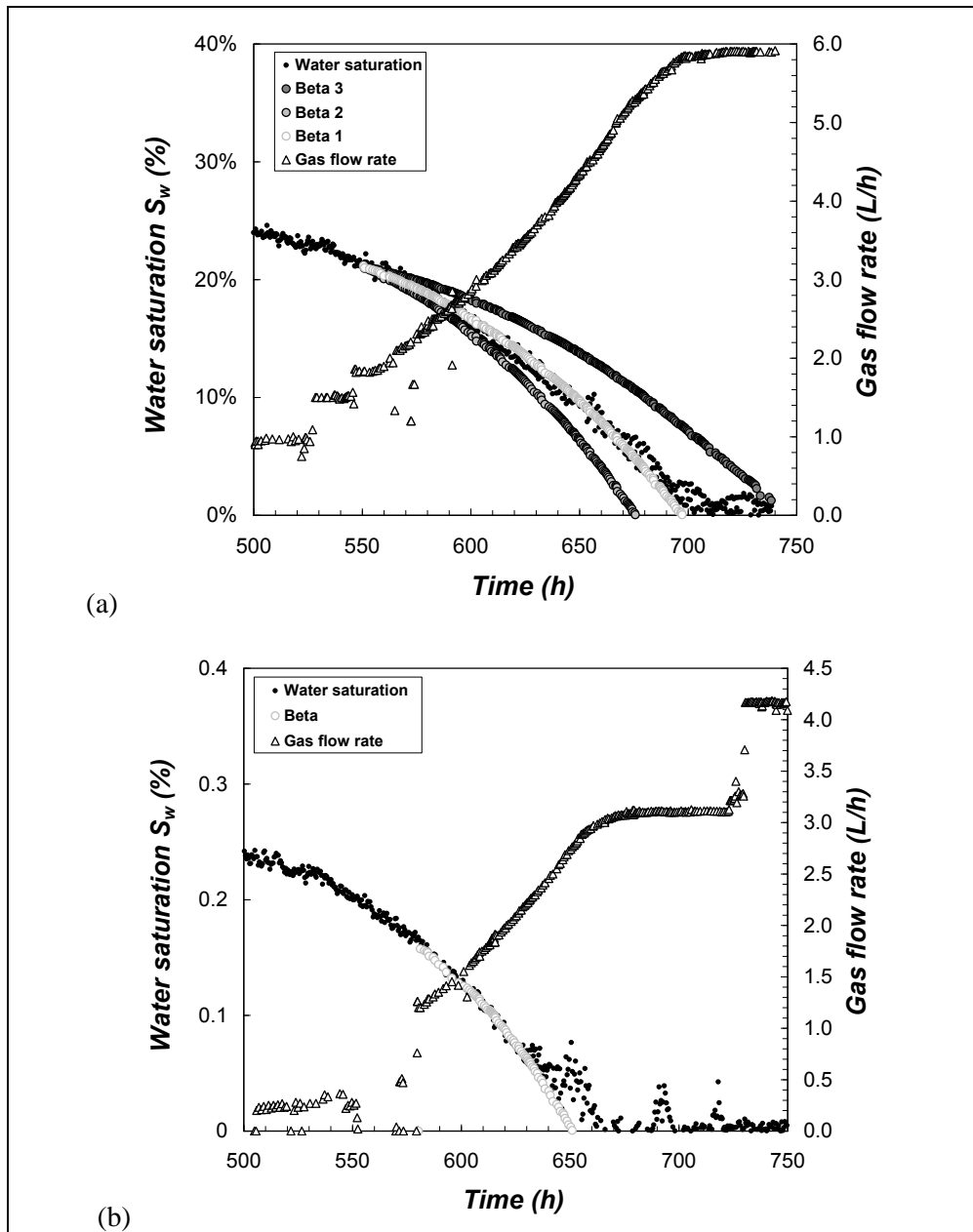


592

593

594

Fig. 7



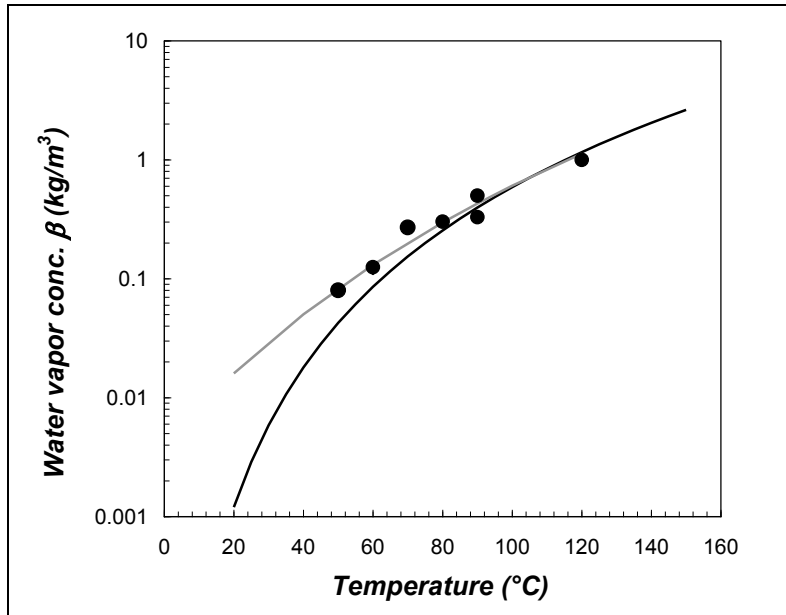
595

596

597

598

Fig. 8

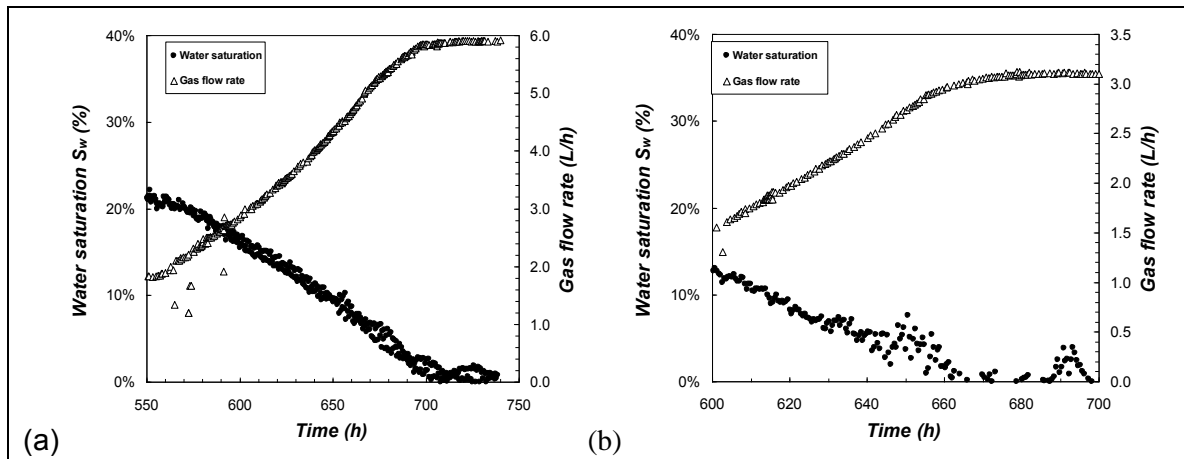


599

600

601

Fig. 9

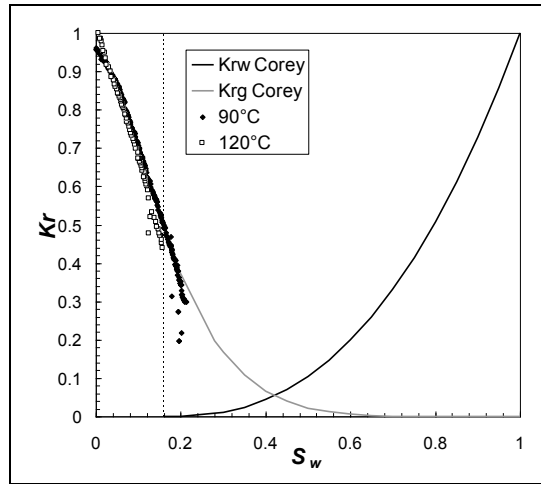


602

603

604

Fig. 10

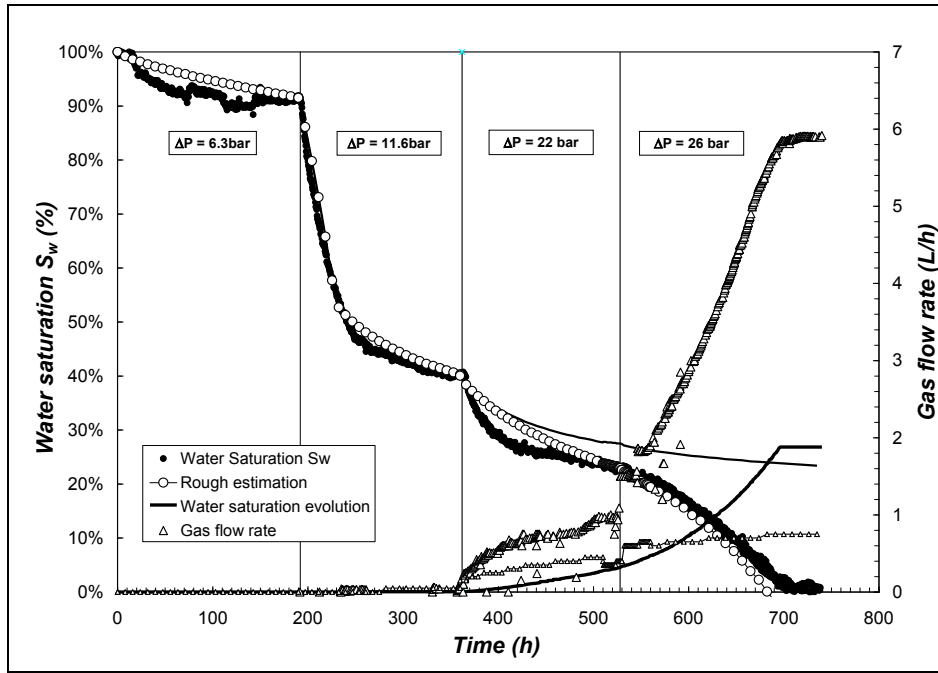


605

606

607

Fig. 11



608

609

610

Fig. 12

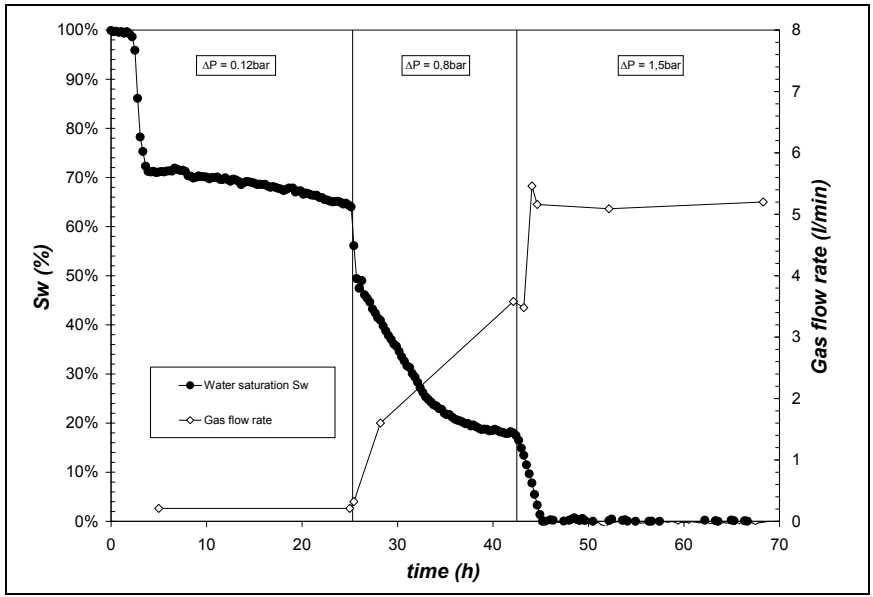
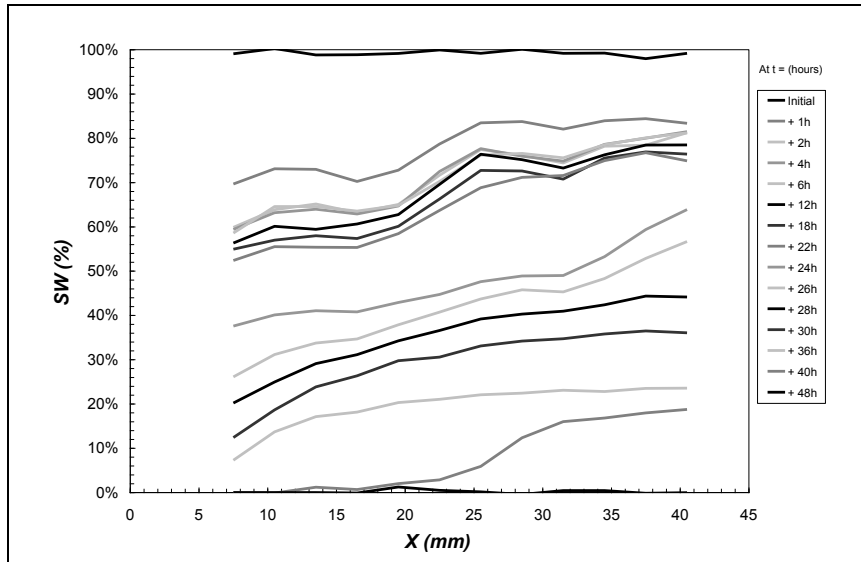


Fig. 13

611

612

613

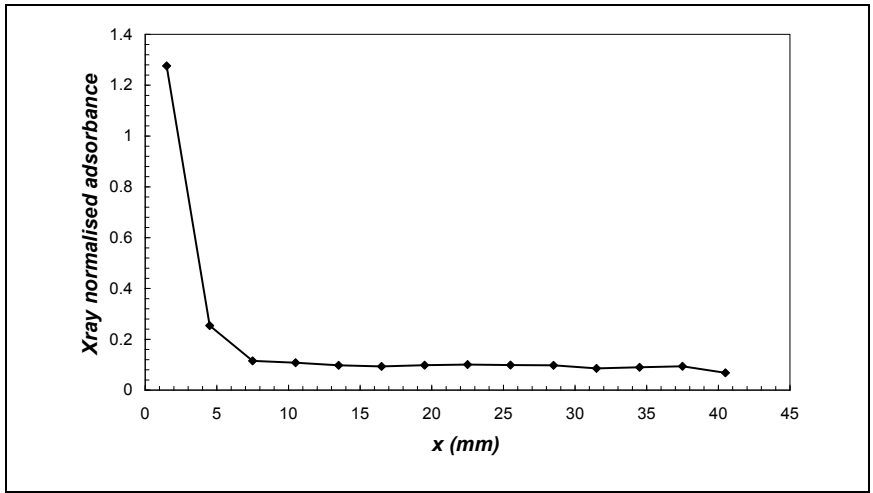


614

615

616

Fig. 14

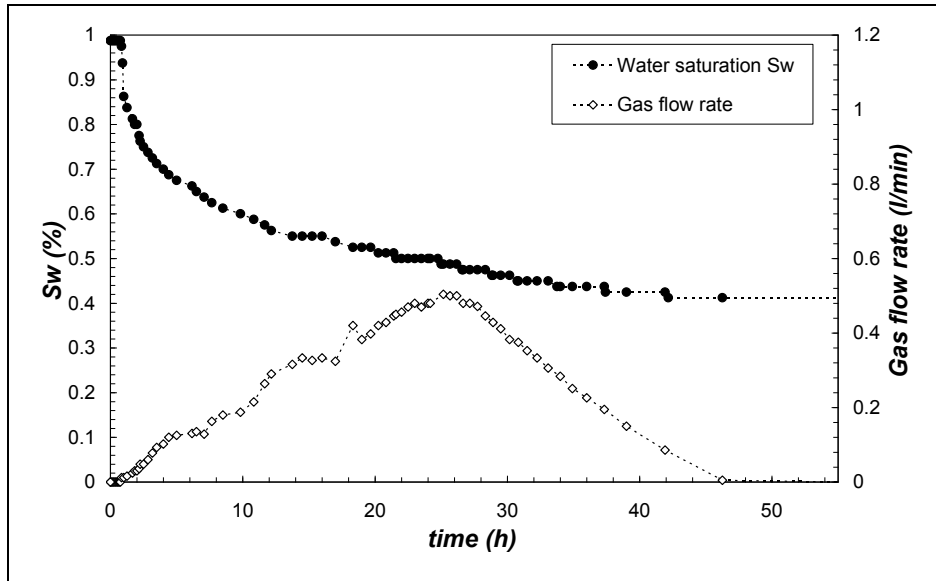


617

618

619

Fig. 15



620

621

622

Fig. 16

623 Table 1: Sample characteristics for each experiment.

<i>Rock Sample</i>	<i>Temperature</i>	<i>Brine</i>	<i>Initial Porosity</i>	<i>Initial permeability</i>	<i>Final permeability</i>
Moliere Sandstone	90°C	Paris basin brine (160g/l TDS)	14%	8 10 ⁻³ mD	3 10 ⁻³ mD
Moliere Sandstone	120°C	Paris basin brine (160g/l TDS)	14%	12 10 ⁻³ mD	6 10 ⁻³ mD
Vosges Sandstone	80°C	KCl + KI (35g/l TDS)	21.8%	74 mD	22 mD
Vosges Sandstone	60°C	KCl (150g/l TDS)	21.8%	160 mD	0 mD

624

625